

Correction of Positional Errors and Geometric Distortions in Topographic Maps and DEMs Using a Rigorous SAR Simulation Technique

Hongxing Liu, Zhiyuan Zhao, and Kenneth C. Jezek

Abstract

In the history of surveying and mapping, a large volumes of topographic maps and digital elevation models have been created at various scales throughout the world. However, positional errors and geometric distortions may exist in the topographic contour maps and their derived DEMs due to inaccurate ground control and poor navigation techniques in the early years. In this paper, we present a new technique to detect and correct positional errors and geometric distortions in topographic data based on rigorous Synthetic Aperture Radar (SAR) image simulation and mathematical modeling of SAR imaging geometry. Our method has been successfully applied to two USGS topographical data sets in Antarctica. Using Radarsat SAR imagery, positional errors of these two data sets have been reduced from 5 km to 200 m and from 200 m to 50 m, respectively.

Introduction

Traditionally, terrain is depicted by topographic maps with contour lines. Over the last hundred years, numerous topographic maps at various scales have been produced by various mapping agencies, such as the USGS (USGS, 1999). With rapid advances in computer technology, the raster-based Digital Elevation Model (DEM) has replaced topographic maps for collecting, storing, and conveying surface topography information. Recent decades have witnessed a rapid growth in DEM production. Due to their low-cost and wide availability, the contour data digitized from topographic maps were often used as the primary input data source, for example, USGS DEM products (USGS, 1987 and 2000). Consequently, positional errors and geometric distortions that exist in the early topographic maps were propagated into the DEMs. The presence of positional errors and geometric distortions often causes geographic misplacement of topographic features, inhibits the alignment and co-registration of topographic data with other geo-spatial data layers, and hence, plagues subsequent spatial data integration and modeling. The development of the global positioning system (GPS), inertial navigation system (INS), and new topographic data

acquisition techniques, such as digital photogrammetry based on automated image matching (Miller and Helava, 1992; Heipke, 1992; Mikhail, *et al.*, 2001), Interferometric SAR (INSAR) (Goldstein, *et al.*, 1993; Zebker, *et al.*, 1994) and Light Detection and Ranging (LIDAR) systems (Hill, *et al.*, 2000; Flood, 2001) technologies, have greatly improved the precision of planimetric positioning, as well as, the vertical accuracy of newly acquired elevation measurements. However, to fully utilize the existing topographic data, it is desirable to develop a technique to handle positional errors and geometric distortions.

This paper presents a new method for detecting and correcting positional errors and geometric distortions in the existing topographic contour maps and their derived DEMs based on a Synthetic Aperture Radar (SAR) image simulation technique. With Radarsat-1 SAR image data captured in 1997, we analyzed two topographic data sets in the Ellsworth Mountains and Dry Valley regions, Antarctica, which were originally produced by the USGS in the 1960s and 1970s using aerial photogrammetric techniques. Our analysis reveals a planimetric positional error as large as 5 km for topographic features. It was found that the positional shifts are not systematic, and consequently, the shape of the terrain was geometrically distorted. Using rigorous SAR image simulation and mathematical modeling of SAR imaging geometry, we successfully corrected the positional errors and geometric distortions in these topographical data sets.

In the following sections, we first describe the algorithms and processing steps involved in our method, then, demonstrate the effectiveness of our methods through two application examples, and finally, present some technical remarks and conclusions.

Methodology

Overview

Image simulation refers to the digital synthesis of an image, based on topographic data with a prescribed illumination position, imaging geometry, as well as, an assumption regarding the reflectance or backscattering properties of the ground in the scene. Due to the side-looking geometry and complex backscattering mechanisms, radar image simulation is more

H. Liu is with the Department of Geography, Texas A&M University, College Station, TX 77843 (liu@geog.tamu.edu).

Z. Zhao is with Atlantis Scientific Inc., 20 Colonnade Road, Suite 110, Nepean, Ontario, K2E 7M6, Canada (zhiyuan.zhao@atlantis-scientific.com).

K.C. Jezek is with the Byrd Polar Research Center, The Ohio State University, Columbus, OH 43210 (jezek@frosty.mps.ohio-state.edu).

Photogrammetric Engineering & Remote Sensing
Vol. 70, No. 9, September 2004, pp. 1031–1042.

0099-1112/04/7009-1031/\$3.00/0
© 2004 American Society for Photogrammetry
and Remote Sensing

complicated and challenging, compared with optical image simulation. Since the radar image simulation technique was first proposed by Holzman and his associates (Holzman, *et al.*, 1978), it has been used in a variety of applications. For example, many investigators employed the SAR image simulation technique to examine the effects of varying radar system parameters (wavelength, polarization, and resolution) and imaging geometry configuration (incidence angle, look direction, satellite heading, and altitude) for the purpose of evaluating the proposed design of radar sensors or future image acquisition plans (Domik, *et al.*, 1986; Nasr and Vidal-Madjar, 1991; Guindon, 1993). In addition, SAR image simulation techniques have been effectively used to determine the optimum stereo intersection geometry from various candidate configurations (Kaupp, *et al.*, 1983; Kobrick, *et al.*, 1986; Leberl, 1990 and 1998). Radar image simulation was also frequently used to identify Ground Control Points (GCPs) for geocoding and terrain correction of SAR imagery (Guindon and Maruyama, 1986; Kwok, *et al.*, 1990; Arai, 1991; Guindon, 1995; Polidori, 1998). In most previous applications, input topographic data were assumed to be free of positional errors and provided sufficient topographical details.

Different from previous applications, we attempt to detect and correct positional errors in historic topographic data with the image simulation technique. Our method is based on two observations. First, most historic topographic maps were created based on photogrammetric processing of aerial photographs. Although the vertical measurements of the elevation are quite accurate, serious positional errors may exist due to a variety of reasons, such as, poor navigation technology for aerial photography in the early years, lack of high-quality ground control points in the remote and inaccessible regions, and the prevailing hostile environment and weather conditions when surveying and mapping projects were conducted. Second, with the development of differential global positioning system (DGPS) and INS technologies and the densification of a satellite ground tracking station network, the accuracy of satellite orbit ephemeris data has been greatly improved. The three-dimensional position and velocity of a spaceborne platform can be determined with very high accuracy, and the attitude of the sensor can also be measured with considerable accuracy. Consequently, the geo-locations of satellite image pixels derived from the satellite orbit ephemeris data are quite accurate. In the case of Radarsat imagery, the positional accuracy of satellite image pixels is somewhat more than 200 m with the original satellite ephemeris data (Jezek, 2003). A post-processing procedure based on the block adjustment technique can further refine the satellite ephemeris data. To refine the satellite orbit ephemeris, four or more GCPs are required for a group of satellite orbits with over a hundred frames. Through the block adjustment, the refined ephemeris data can be re-propagated and applied to each orbit, including the orbits and orbit segments where no GCPs are available. For example, the geolocation accuracy of Radarsat SAR imagery is better than 50 m with the satellite ephemeris data refined by the block adjustment method (Jezek, 2003). Clearly, image data captured by the current generation of satellite sensors can be used to correct positional errors and geometric distortions in historic topographic data.

We chose to utilize spaceborne SAR image data in our analysis because a large quantity of high-resolution SAR image data is available for our case study areas in Antarctica. SAR sensors are capable of penetrating clouds and imaging the earth's surface day and night independent of solar illumination. In contrast, cloud-free and non-saturated optical satellite images are relatively difficult to acquire in Antarctica due to long polar nights, cloudy weather, and ice and snow-covered surface.

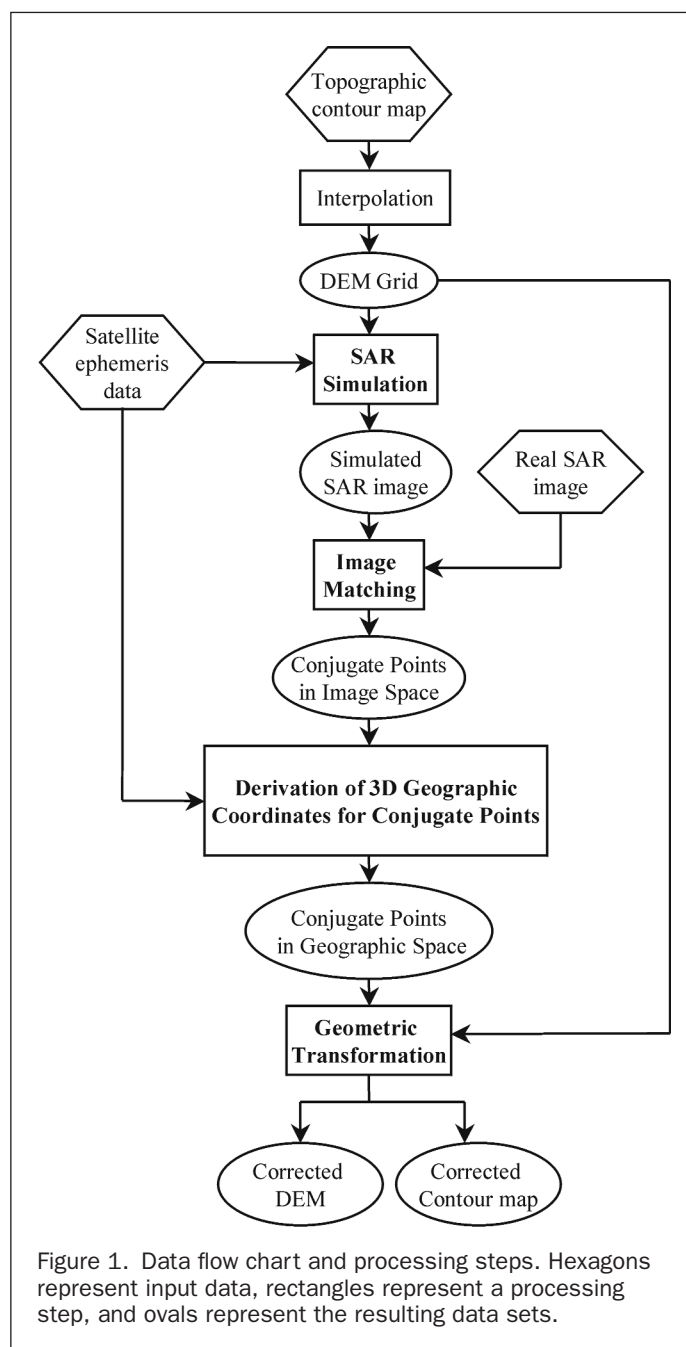


Figure 1. Data flow chart and processing steps. Hexagons represent input data, rectangles represent a processing step, and ovals represent the resulting data sets.

As shown in Figure 1, our method consists of four major processing steps: SAR image simulation based on the given topographic data and satellite ephemeris data; identification of conjugate (tie) points by matching the simulated image and real SAR image in the slant range image space; derivation of 3D coordinates for the conjugate (tie) points in the geographic space; and geometric correction of the topographic data using a local piecewise transformation. The input data required for our method include the topographic data under investigation (digitized contours or a DEM), a slant-range SAR image and the associated meta data about satellite ephemeris.

Rigorous SAR Image Simulation

The synthesis of a slant range SAR image is based on the topographic data and the state vector of the radar sensor at the time the real SAR image was acquired. A spaceborne SAR sensor is

an active microwave imaging system. It illuminates the ground surface in a side-looking geometry by radar pulses and then coherently records the echoed signals. To closely emulate the characteristics of the real SAR image, we employ a rigorous simulation procedure, which takes into account both the motion of the SAR sensor and geometric distortions due to the earth rotation, earth curvature, and topographic effects (lay-over, foreshortening, and radar shadows).

Since positional errors and geometric distortions exist in topographic data, the real SAR image cannot be terrain-corrected before these errors and distortions are corrected. Therefore, we can only correlate and match the synthesized image and the uncorrected real SAR image in the slant range-azimuth image coordinate system, instead of, a map projection coordinate system.

In our analysis, the available topographic data source is a digitized contour map. It is interpolated into a regularly spaced DEM using a two-stage TOPOGRID method (Liu, *et al.*, 1999).

The simulation algorithm maps each cell of the DEM to an image pixel in the slant range geometry, and two operations are involved. First, the row and column numbers (i, j) of the image pixel corresponding to a given DEM cell are computed based on the SAR model. Second, the backscattered power (brightness value) σ is calculated for the pixel using a simplified backscattering model.

Calculation of Image Coordinates in a Slant Range Image Space

A DEM (or topographic contour map) is commonly referenced to a specific map projection and coordinate system. To reconstruct the SAR imaging geometry, we need to transform map projection coordinates (x, y) and elevation values h of the DEM cells into three-dimensional coordinates in an earth-centered Cartesian coordinate system. After transformation, each DEM cell (x, y, h) corresponds to a target point $P(X, Y, Z)$ in the 3D Cartesian coordinate system (Figure 2). Given a DEM cell, $P(X, Y, Z)$ we need to determine its two-dimensional image coordinates: row and column number, (i, j). In slant range geometry, the image row number i is known as the azimuth (along-track) coordinate, while the image column number j is known as the slant range (cross-track) coordinate. With the known sensor position and velocity vector, we can form two

equations for each DEM cell, $P(X, Y, Z)$, in a geocentric inertial Cartesian coordinate system (Curlander, *et al.*, 1987; Meier, *et al.*, 1993):

$$R(t) = \sqrt{(\vec{S}(t) - \vec{P}(t)) \cdot (\vec{S}(t) - \vec{P}(t))} \quad (1)$$

$$f_D(t) = \frac{2}{\lambda R(t)} (\vec{V}_s(t) - \vec{V}_p(t)) \cdot (\vec{S}(t) - \vec{P}(t)) \quad (2)$$

where $\vec{P}(t) = (X, Y, Z)$ is the known position of a DEM cell in 3D Cartesian coordinate system; t is the time when the DEM cell is imaged; $\vec{S}(t) = (X_s, Y_s, Z_s)$ is the sensor position at the time t ; $\vec{V}_p(t) = (\dot{X}, \dot{Y}, \dot{Z})$ is the velocity vector of the DEM cell due to the earth's rotation; $\vec{V}_s(t) = (\dot{X}_s, \dot{Y}_s, \dot{Z}_s)$ is the velocity vector of the sensor, which is determined by the attitude angles and moving speed of the radar sensor along the orbit; $R(t)$ is slant range from the sensor to the DEM cell; $f_D(t)$ is the Doppler frequency shift of the DEM cell; λ is the radar wavelength; and the dot ($\dot{\cdot}$) denotes the inner product of vectors.

The range equation (1) determines a range sphere with radius $R(t)$, meaning that the ground target point, $P(X, Y, Z)$, must lie on this sphere centered at the sensor. The Doppler equation (2) describes a Doppler cone whose vertex is at the sensor, meaning that the target point must be located along the cone. The Doppler centroid f_{DC} is given by the equation (Leberl, 1990):

$$f_{DC} = \frac{2 |\vec{V}_s - \vec{V}_p|}{\lambda} \sin \tau \quad (3)$$

where τ is the squint angle, which is the angle between the line connecting the sensor/ground target and the zero Doppler plane (the perpendicular direction to the SAR moving direction). When the squint angle is zero, the Doppler centroid becomes the zero Doppler. In this case, the Doppler cone is fully opened and degenerates to a plane.

At the time the radar-beam centroid intersects the DEM cell, the Doppler shift $f_D(t)$ equals the Doppler centroid f_{DC} . Therefore, the imaging time t for the DEM cell can be determined by the following equation:

$$f_D(t) - f_{DC} = \frac{2}{\lambda R(t)} (\vec{V}_s - \vec{V}_p) \cdot (\vec{S} - \vec{P}) - f_{DC} = 0. \quad (4)$$

Since Equation 4 is nonlinear in terms of the unknown time t , it is generally impossible to solve the equation directly. We apply the Newton-Raphson method to iteratively find the solution for the time t that leads to the right Doppler shift to satisfy Equation 4. Given the initial value t_0 , one round of iteration is defined by the following equations (Olmsted, 1993):

$$t_1 = t_0 + \Delta t \quad (5)$$

$$\Delta t = (f_D(t_0) - f_{DC}) / \frac{df_D(t_0)}{dt} \quad (6)$$

$$\frac{df_D(t)}{dt} = -\frac{2}{\lambda R(t)} \left((\vec{S} - \vec{P}) \cdot (\vec{A}_s - \vec{A}_p) + (\vec{V}_s - \vec{V}_p) \cdot (\vec{V}_s - \vec{V}_p) - \left(\frac{(\vec{S} - \vec{P}) \cdot (\vec{V}_s - \vec{V}_p)}{R(t)} \right)^2 \right) \quad (7)$$

where $\vec{A}_p = (\ddot{X}, \ddot{Y}, \ddot{Z})$ is the acceleration vector of the DEM cell, and $\vec{A}_s = (\ddot{X}_s, \ddot{Y}_s, \ddot{Z}_s)$ is the acceleration vector of the sensor along the orbit. The calculated Doppler frequency shift $f_D(t_0)$ is compared with the Doppler centroid f_{DC} in Equation 6 to determine the time correction term Δt for the next iteration.

As the SAR sensor continuously moves along an orbit during image acquisition, the instantaneous sensor state vector: $\vec{S} = (X_s, Y_s, Z_s)$, velocity vector: $\vec{V}_s = (\dot{X}_s, \dot{Y}_s, \dot{Z}_s)$, and

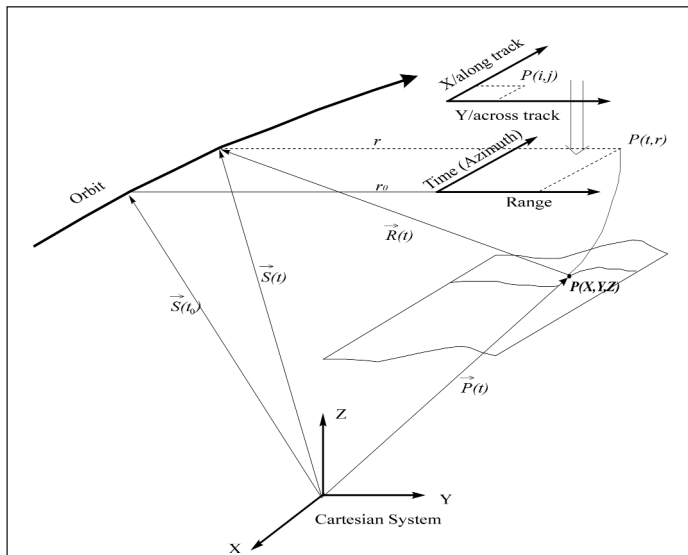


Figure 2. 3D Cartesian coordinate system and SAR imaging geometry.

acceleration vector: $\vec{A}_s = (\ddot{X}_s, \ddot{Y}_s, \ddot{Z}_s)$ are time-dependent and can be modeled through a polynomial equation. Given the three sets of position vectors for start, center, and end of the imaging period for satellite ephemeris, the instantaneous sensor position is modeled by (Olmsted, 1993; Raggam, *et al.*, 1993):

$$\vec{S}(t) = \begin{cases} X_s = a_0 + a_1t + a_2t^2 + a_3t^3 \\ Y_s = b_0 + b_1t + b_2t^2 + b_3t^3 \\ Z_s = c_0 + c_1t + c_2t^2 + c_3t^3 \end{cases} \quad (8)$$

where a_i, b_i, c_i ($i = 1, 2, 3$) are fitted coefficients.

The Doppler centroid varies along azimuth and range direction and can be approximated with the satellite ephemeris data through a polynomial (Olmsted, 1993; Raggam, *et al.*, 1993):

$$f_{DC} = d_0 + d_1R + d_2R^2 + d_3t + d_4t^2 \quad (9)$$

where d_i ($i = 1, 2, 3, 4$) are fitted coefficients; R is the slant range, and t is the time.

In the geocentric inertial coordinate system, the X-axis points in the constant direction of the vernal equinox. For the DEM cell, $P(X, Y, Z)$, its velocity vector relative to an inertial geocentric system can be calculated as:

$$\vec{V}_p = \vec{\omega}_E \times \vec{P} \quad (10)$$

where $\vec{\omega}_E = (0, 0, \frac{2\pi}{23.93447 \text{ hrs}})^T$ is the angular velocity of the Earth's rotation.

The imaging time t , determined by the Newton-Raphson iteration method, can be converted to the slant range image row number i by using the azimuthal sampling rate:

$$i = \frac{t - t_{\text{offset}}}{\delta t} \quad (11)$$

where t_{offset} is the time offset (time of the first line), and δt is the time spacing between adjacent lines.

By substituting the imaging time t into the polynomial (Equation 8), we can calculate the satellite position $\vec{S}(X_s, Y_s, Z_s)$, and then calculate the slant range $R(t)$ of the DEM cell $P(X, Y, Z)$ from the range (Equation 1). The slant range $R(t)$ can be further converted to the column number j in the slant range image:

$$j = \frac{R - R_{\text{offset}}}{\delta R} \quad (12)$$

where R_{offset} is the range offset (range of the first sample), and δR is the pixel spacing in the range.

Symbolically, the geometric position determination in the SAR image simulation can be expressed as: $(x, y, h) \rightarrow (X, Y, Z) \rightarrow (t, R) \rightarrow (i, j)$. Namely, we first reconstruct the SAR imaging geometry with satellite ephemeris data, and then find the slant range image coordinates (i, j) for each DEM cell $P(X, Y, Z)$ using the rigorous SAR model.

Calculation of Image Intensity Value

SAR image brightness values represent the backscattered power of a radar signal. According to the radar equation (Leberl, 1990; Curlander and McDonough, 1991), the magnitude of the returned power can be decomposed into system effect and terrain effect. For a specific SAR system, the system effect can be regarded as a constant. The terrain effect can be further split into two components: the differential scattering cross-section per unit area (backscatter coefficient) and the illuminated area of the resolution cell. Previously, the generalized cosine model (Keydel, 1982), Hagfors model (Leberl, 1990), and Muhleman model (Leberl, 1990) have been used in the literature to approximate the relationship of returned radar power with the local incidence angle. In our simulation, we adopt a modified

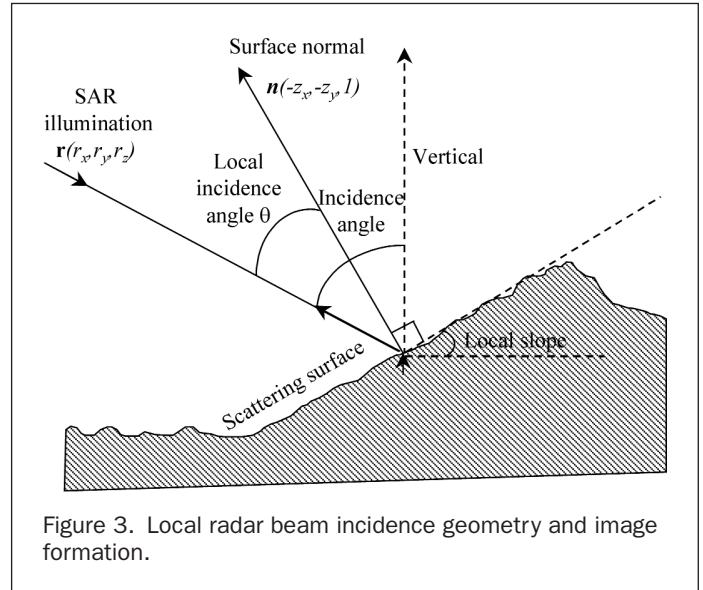


Figure 3. Local radar beam incidence geometry and image formation.

version of Muhleman backscatter model (Wivell, *et al.*, 1992; Leberl, 1998):

$$\sigma = \log \left[\frac{M^3 \cos \theta}{(\sin \theta + M \cos \theta)^3} \right] \quad (13)$$

where θ is the local incident angle, and M is a constant coefficient. The local incidence angle θ is defined by the local surface normal and the radar illumination vector (slant range vector) as shown in Figure 3.

In the modified Muhleman backscatter model, the cosine of the local incidence angle is used to approximate the radar cross section (Holecz, *et al.*, 1993):

$$\cos \theta = \vec{r} \cdot \vec{n} = \frac{-z_x r_x - z_y r_y + r_z}{\sqrt{z_x^2 + z_y^2 + 1}} \quad (14)$$

where $\vec{r} = (r_x, r_y, r_z)$ is the unit vector of the SAR illumination direction vector, and $\vec{n} = (-z_x, -z_y, 1)$ is the surface normal vector; z_x and z_y are surface slopes along the range (x) and azimuth (y) directions. For each DEM cell, its four neighboring cells are included for the calculation of the component surface slopes in the surface normal vector.

By comparing the SAR sensor look angle and the calculated surface slope, we are also able to create the layover and shadowing masks (Figure 4) (Kropatsch and Strobl, 1990;

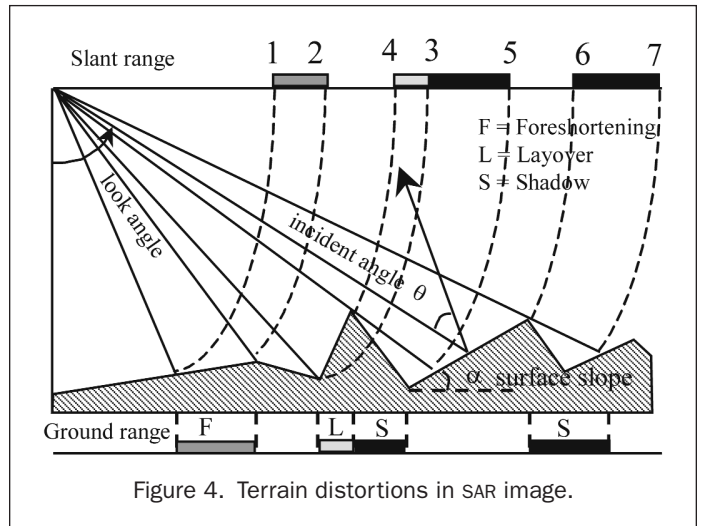


Figure 4. Terrain distortions in SAR image.

Olmsted, 1993), which are excluded from the subsequent image matching operation. Foreshortening and layover will induce a many-to-one mapping, namely, many surface points (DEM cells) may be mapped onto one pixel (i, j) in the slant range image. In this case, the radiometric value assigned to pixel (i, j) is a summation of backscatters from all DEM cells that are geometrically mapped to (i, j) . For a DEM cell that is mapped onto a pixel in the radar shadow, zero power return is assigned for the pixel. Geometric and radiometric processing of all the DEM cells result in a two-dimensional array of the backscattered power, namely, the simulated slant range SAR image.

To increase the radiometric quality, the simulated image is calibrated by matching its histogram to that of the real SAR image. This improves the image matching operation described in the following section.

Identification of Conjugate Points by Image Matching

Image matching is performed between the simulated image and the real SAR image. This process starts with manual selection of a set of initial conjugate (tie) points, followed by an automated image matching procedure. Manual selection of conjugate points is interactively performed with the aid of a graphic tool in the ERDAS. Imagine environment. Then, we use an area-based image matching method (Fonseca and Manjunath, 1996; Schenk, 1999) to refine the conjugate points. For each candidate point, a small image chip is extracted around the candidate as the reference window. A search window with a larger size scans the corresponding part of the original real SAR image. The cross-correlation coefficients are calculated for all pixels in the search window. By fitting a second order polynomial on the correlation coefficient surface, we identify the peak correlation point as the conjugate point at sub-pixel accuracy.

Using the image matching process, we generated a set of conjugate (tie) point pairs: $\{(i, j), (i', j')\}$. (i, j) are the row (azimuth) and column (slant range) coordinates of a geographic feature in the simulated slant range image, and (i', j') are the row and column coordinates of the same geographic feature in the real slant range SAR image. We layered the shadow and layover masks onto the simulated image to avoid the selection of candidate matching points in the radar shadows and layover regions.

Derivation of 3D Geographical Coordinates of Conjugate Points by Space Resection

If the DEM is accurate and free of positional error and if the state vector of SAR sensor determined from the satellite ephemeris data is sufficiently accurate, the coordinates (i, j) of a conjugate point in the simulated image should be exactly the same as its coordinates (i', j') in the real SAR image. However, if a significant difference exists between (i, j) and (i', j') , it would be certain that positional errors exist in the DEM, or the state vector of the SAR sensor supplied with the satellite ephemeris is not accurate. In previous applications, the DEMs were assumed to be accurate and free of positional errors, and geometric positions (i, j) of conjugate points in the simulated SAR image were considered correct and accurate. Following this logic, the conjugate (tie) points inherited the geographic positions of the corresponding DEM cells and were subsequently used as ground control points to refine the satellite state vector for geocoding and terrain correction of the real SAR image (Guindon and Maruyama, 1986; Kwok, *et al.*, 1990; Arai, 1991; Guindon, 1995; Polidori, 1998).

Our method is designed to handle a situation, where satellite orbit ephemeris data are sufficiently accurate, but positional errors and geometric distortions occur in the DEM created from historic data sources. In this case, we ascribe the possible misalignment of topographic features in the simulated and real SAR image to the positional errors in the DEM rather than the inaccuracy of satellite orbit ephemeris

data. In other words, for a conjugate point pair we consider its row (azimuth) and column (slant range) coordinates (i', j') in the real SAR image to be accurate and correct, but their corresponding row and column coordinates (i, j) in the simulated image are subject to error due to the positional errors in the DEM. The purpose of image matching is to determine the correct three-dimensional geographic coordinates, $P'(X', Y', Z')$, for each conjugate point, given its correct image coordinates, (i', j') . This is the inverse process of the SAR image simulation.

With the image coordinates, (i', j') , of the conjugate point, we can form two equations: the range equation and the Doppler equation. By rewriting the range and Doppler equations for each conjugate point, we obtain:

$$(X' - X_s)^2 + (Y' - Y_s)^2 - (Z' - Z_s)^2 = R^2 \quad (15)$$

$$\begin{aligned} &(\dot{X}' - \dot{X}_s)(X' - X_s) + (\dot{Y}' - \dot{Y}_s)(Y' - Y_s) + (\dot{Z}' - \dot{Z}_s)(Z' - Z_s) \\ &= \frac{\lambda R f_{DC}}{2} \end{aligned} \quad (16)$$

where $\tilde{P}' = (X', Y', Z')$ is the unknown geographic position of a conjugate point to be solved; $\tilde{S} = (X_s, Y_s, Z_s)$ is the sensor position at the time the conjugate point was imaged; $\tilde{V}_p = (\dot{X}', \dot{Y}', \dot{Z}')$ is the velocity vector of the conjugate point; $\tilde{V}_s = (\dot{X}_s, \dot{Y}_s, \dot{Z}_s)$ is the velocity vector of the sensor, which are determined by the attitude angles and moving speed of the sensor along the orbit; and R is the slant range from the sensor to the conjugate point. For each conjugate point, the slant range, the imaging time, the SAR sensor position and velocity, and the Doppler centroid can be determined based on its image coordinates, (i', j') , in the real SAR image. The slant range R is calculated from the image column number j' using Equation 12. The imaging time t for the conjugate point is computed from the image row number i' using Equation 11. By substituting imaging time t into the fitted orbital polynomial model (8), we obtain the sensor position vector, $\tilde{S} = (X_s, Y_s, Z_s)$, and then the velocity vector, $\tilde{V}_s = (\dot{X}_s, \dot{Y}_s, \dot{Z}_s)$. The Doppler centroid f_{DC} is determined from the fitted polynomial, Equation 9.

However, two equations are not sufficient to solve the three unknown geographic coordinates, (X', Y', Z') , of the conjugate point. In a stereo configuration, the other real SAR image acquired from a different viewpoint would be used to provide two additional equations, in which the 3D geographic coordinates of the matched point can be over-determined with two range and two Doppler equations. In our case, we only have a single real SAR image. To solve the 3D geographic coordinates, $P'(X', Y', Z')$, for the matched conjugate points, we need to introduce additional information.

As we noted earlier, although positional errors may exist in the historic topographic data, the vertical measurements derived from aerial photogrammetry techniques are quite accurate. Our task is to correct the planimetric coordinates of a DEM cell without the modification of its elevation value. Assume the pixel (i, j) in the simulated image corresponds to a DEM cell (x, y, h) , and the conjugate pixel (i', j') in the real SAR image corresponds to the ground point (x', y', h') . As a conjugate point pair $\{(i, j), (i', j')\}$ represents the same geographic feature, its elevation value h taken from the DEM cell can be assigned to the ground point that maps to the conjugate pixel (i', j') , namely, $h' = h$. With the known elevation value h , we introduce the third equation that constrains the conjugate point to satisfy an earth ellipsoid model (Olmsted, 1993):

$$\frac{X'^2 + Y'^2}{(r_E + h)^2} + \frac{Z'^2}{(1 - f)^2 (r_E + h)^2} = 1 \quad (17)$$

where h is the known elevation, r_E is the equatorial radius of the earth, $f(1/298.255)$ is the flattening factor of the WGS84

ellipsoid, and (X', Y', Z') are unknown geographic coordinates of the conjugate point.

Now, the computational problem can be restated as: given the correct slant range azimuth coordinates (i', j') and the elevation value h of a conjugate point, we derive the 3D geographic position, (X', Y', Z') , of the ground point associated with the conjugate point. With Equations 15, 16, and 17, we are able to solve for three unknowns, (X', Y', Z') .

Since Equations 15, 16, and 17 are non-linear in terms of the unknowns (X', Y', Z') , an iterative method is used to solve the equations. From the initial estimate of the target position (X'_0, Y'_0, Z'_0) , the corresponding imaging geometry and Doppler frequency shift can be calculated. The calculated Doppler frequency shift is then compared with the Doppler centroid f_{DC} to determine the correction terms for adjustment in the next iteration. Geometrically, the correct 3D position (X', Y', Z') of each conjugate point is determined by the resection of the range sphere, the Doppler cone, and an ellipsoid in the geographic space. The calculated 3D geocentric inertial coordinates, (X', Y', Z') , of the conjugate point are then transformed into map projection coordinates (x', y') and an elevation value h . Symbolically, the above computation process can be expressed as a mapping of the conjugate points from 2D slant range image space to 3D geographic space: $(i', j', h) \rightarrow (t, R, h) \rightarrow (X', Y', Z) \rightarrow (x', y', h)$.

Geometric Transformation of Topographic Data Sets

By combining results from SAR image simulation and 3D geographic position derivation, we are able to map a conjugate point pair $\{(i, j), (i', j')\}$ in the 2D slant range azimuth coordinate system to a point pair $\{(X, Y, Z), (X', Y', Z')\}$ in the geocentric inertial Cartesian coordinate system, and further to a point pair $\{(x, y, h), (x', y', h)\}$ in terms of planimetric map projection coordinates and vertical elevation value relative to an ellipsoid. The original planimetric map projection coordinates; (x, y) are subject to positional errors, and (x', y') are the correct planimetric coordinates derived from mathematic modeling of the SAR imaging geometry. The differences between (x, y) and (x', y') define positional error:

$$e = \sqrt{\Delta x^2 + \Delta y^2} = \sqrt{(x - x')^2 + (y - y')^2} \quad (18)$$

where $(\Delta x, \Delta y)$ is the displacement vector for each conjugate point, and e is the magnitude of positional error.

The selection of a geometric correction method is dependent on the magnitude and spatial pattern of positional errors. If the positional shifts (errors) are systematic, a single Affine transformation function can be fitted on a set of conjugate points $\{(x_i, y_i), (x'_i, y'_i)\} (i = 1, 2, \dots, m)$ to correct the whole DEM data set or contour coverage. A two-dimensional affine transformation can account for translation, scale change, rotation, and skew. However, if the positional shifts are not systematic as in our application examples, a rubber-sheeting transformation needs to be constructed to account for the local effect.

To correct non-systematic positional errors and the corresponding geometric distortions in the DEM or contour coverage, we adopt a local piecewise linear transformation based on Delaunay triangulation (Saalfeld, 1985; Goshtasby, 1986). Given the coordinates of conjugate points in the map projection coordinate system, the DEM or vector contour coverage is first divided into triangular regions by triangulating the conjugate points based on Delaunay criteria (Tsai, 1993). For each triangle, a linear transformation function is then fitted locally:

$$\begin{cases} x'_1 = A + Bx_1 + Cy_1 \\ y'_1 = D + Ex_1 + Fy_1 \\ x'_2 = A + Bx_2 + Cy_2 \\ y'_2 = D + Ex_2 + Fy_2 \\ x'_3 = A + Bx_3 + Cy_3 \\ y'_3 = D + Ex_3 + Fy_3 \end{cases} \quad (19)$$

where A, B, C, D, E, F are transformation parameters, and $\{(x_1, y_1), (x'_1, y'_1)\}, \{(x_2, y_2), (x'_2, y'_2)\},$ and $\{(x_3, y_3), (x'_3, y'_3)\}$ are the known coordinates of conjugate points at the triangle corners. Then, the DEM and topographic contour coverage are geometrically transformed in a piecewise manner from triangle to triangle. In order to transform the entire DEM data set or vector contours, the convex hull, defined by connecting the outer boundary of the conjugate points, should cover the DEM or contour coverage. The piecewise geometric transformation corrects the positional errors and geometric distortions in the contour coverage and its derived DEM, and it ensures the precise co-registration of the corrected DEM with the real SAR image.

Application Examples

We implemented our method using C-programming language, and source codes are available upon request. We used and modified some routines from the ASF STEP tool (Olmsted, 1993) for coordinate system transformations and map projections involved in SAR simulation. Our method has been used to correct positional errors and geometric distortions in topographic data sets of Antarctica in support of the NASA pathfinder project-Radarsat Antarctic Mapping Project (RAMP).

The Antarctic continent is covered by permanent ice and snow cover with a small portion (about 3 percent) of rock outcrops. Optical sensors are affected by clouds and the imagery is often saturated due to the high albedo of snow for visible wavelengths which limits their use in polar regions. With abilities to penetrate through clouds and observe day and night, space-borne SAR sensors can provide high resolution radar imagery over the Antarctic continent. Virtually no vegetation cover and human structures in the continent makes the SAR imagery dominated by topographical effects and surface roughness. This facilitates the image matching operation between topographically simulated SAR images and real SAR images.

During the first Antarctic Image Campaign (AIC-1) in 1997, the Canadian Radarsat-1 SAR sensor imaged the entire Antarctic continent at a 25 meter resolution (Jezek, 1999). The objective of RAMP was to create a seamless ortho-rectified SAR image mosaic of Antarctica, in which digital elevation data are required to process individual SAR images for terrain correction. Various topographical data sources were compiled to generate a digital elevation model over the entire Antarctic continent for this project (Liu, *et al.*, 1999). For mountainous areas, including the Antarctic Peninsula, the Ellsworth Mountains, and the Transantarctic Mountains, the primary topographic data sources are the contour lines digitized from historic topographic maps. Although the digital elevation models derived from the contour maps contain considerable topographic details, serious position errors and geometric distortions were detected in some of these data sets. The essential prerequisite for terrain correction is the precise co-registration between digital elevation data and SAR image data. The presence of positional errors and geometric distortions in the topographic data caused the misalignment of elevation data with the SAR images, resulting in serious deformations and smearing of terrain features on the SAR images during the orthorectification process (Jezek, *et al.*, 2000).

The occurrences of serious positional errors are mainly due to the poor aerial navigation technique and lack of quality GCPs at the time the survey and mapping projects were conducted. Since the continent is so close to the south magnetic pole, compasses behave erratically. It was reported that there were no aids to aerial navigation except fleeting glimpses of the sun in the early years, and that most of the astronomical points for geolocating a position either failed to work or produced inexact results in these high southern latitudes (Larsgaard, 1993). Due to the constant motion of ice and snow and the vast expanses of featureless surfaces, it was very difficult to find stable geodetic control points upon which

aerial photography for mapping must be based. In addition, the brutal weather conditions, especially the frequent and often enduring blizzards, made the survey and mapping work extremely difficult to achieve a high accuracy in Antarctica (Larsgaard, 1993).

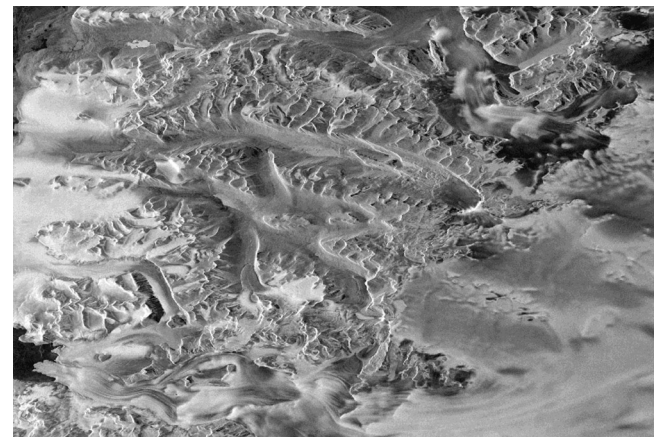
To fully utilize the valuable historic topographical data, we employed the Radarsat-1 SAR imagery captured in 1997 to correct the positional errors and geometric distortions in the topographic data. Prior to the Antarctic Imaging Campaign, a radar transponder was deployed at the South Pole using GPS technology, which was operated throughout the mission as a geographic reference point for the Radarsat-1 SAR sensor. A set of GCPs with accuracy on the order of about 25 m was also acquired for the RAMP project in areas with rock outcrops and nunataks along the coast (Jezek, 2003). A block adjustment tool developed by the Vexcel Corporation uses the transponder, GCPs, and swath-to-swath tie points as input to adjust the satellite ephemeris data (position and velocity vectors of radar sensor) for a group of orbits in a block, which consists of about 150 image frames. Each image frame covers a ground area of $100 \text{ km} \times 100 \text{ km}$. Recognizable image features are selected over the overlap regions of adjacent orbits as orbit-to-orbit tie points, which are used to perform relative orientation of the image frames from one orbit to other orbits in the block. It should be pointed out that the orbit ephemeris refinement based on the block adjustment requires only four GCPs for each block (with about 150 image frames), far fewer than conventional frame-by-frame geocoding operations. A comparison with the reserved checkpoints shows that the geolocation of terrain features in SAR imagery derived from original satellite ephemeris data is accurate to about 200 m. With the refined satellite ephemeris data, the Root Mean Squared Error (RMSE) of SAR imagery can be reduced to about 50 meters (Jezek, 2003). Therefore, the real SAR image with the adjusted satellite orbit ephemeris data warrants the detection and correction of positional errors in the topographic data that are larger than 50 m.

Correction of Topographic Data in the Dry Valley Region, Antarctica

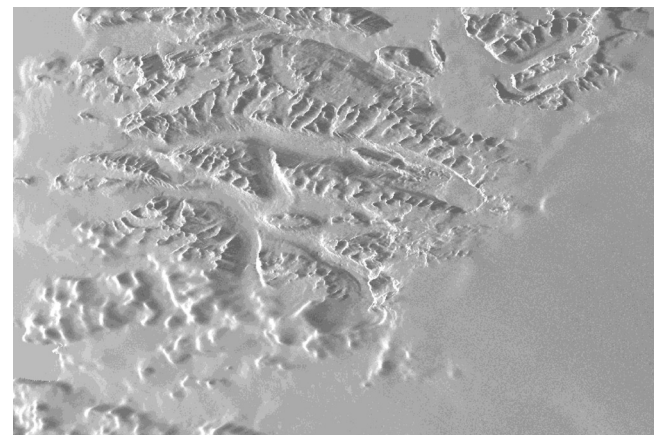
The topographical contour map in the Dry Valley region was digitized from USGS topographical maps at 1:50000 scale, which were photogrammetrically generated in 1975 from US Navy aerial photographs. The McMurdo Dry Valleys are located in the Transantarctic Mountains, and its terrain is characterized by rugged valleys and alpine glaciers. The SAR image for this region was acquired by the Radarsat-1 sensor on 01 October, 1997 with Standard Beam 2 (Figure 5a). The characteristics of the SAR image are listed in Table 1 covering a ground area about $100 \text{ km} \times 100 \text{ km}$.

TABLE 1. CHARACTERISTICS OF SAR IMAGES USED FOR ELLSWORTH MOUNTAINS AND DRY VALLEYS

Characteristics	Dry Valley Scene	Ellsworth Mountains Scene
Acquisition Date	October 1, 1997	September 29, 1997
Latitude at scene center	77.41°S	78.12°S
Longitude at scene center	160.96°E	86.14°W
Orbit	Ascending	Ascending
Wavelength	C-band (5.6 cm)	C-band (5.6 cm)
Radar beam	Standard 2	Standard 2
Incidence angle at scene center	28.25°	28.25°
Azimuth resolution	25 m	25 m
Slant range resolution	8.117 m	8.117 m
Image samples	6250	6250
Image lines	4096	4096
Ground coverage	about $100 \times 100 \text{ km}$	about $100 \times 100 \text{ km}$



(a)



(b)

Figure 5. Real and simulated SAR images of the Dry Valley. (a) real slant range SAR image; (b) the simulated slant range SAR image (the blurred portion is derived from a 1:250000 scale map).

The digitized contour coverage was interpolated into a digital elevation model in grid format using a modified two-stage TOPOGRID method (Liu, *et al.*, 1999). The digital elevation model is in the Polar Stereographic map projection referenced to WGS84 ellipsoid. Using the four corner points of the SAR image, the digital elevation model is clipped and resampled to match the spatial resolution of the SAR image.

Based on the digital elevation model and the satellite orbit ephemeris data, a slant range SAR image is geometrically and radiometrically simulated under the same imaging condition as the real SAR image (Figure 5b). As the topographic data in the Dry Valleys were derived from a large-scale topographic map, the simulated slant range SAR image has a high resolution (Figure 5b). This enables us to identify a dense set of conjugate points (Figure 6).

Through image matching between the simulated and real SAR images, we identified conjugate points in the slant range azimuth image space. Based on the slant range image coordinates of conjugate points in the real SAR image and their corresponding elevation values taken from the DEM, we computed the correct 3D geocentric Cartesian coordinates for each conjugate point by mathematical modeling of SAR imaging geometry. These coordinates are then transformed to Polar Stereographic map projection coordinates and WGS84 ellipsoid heights.

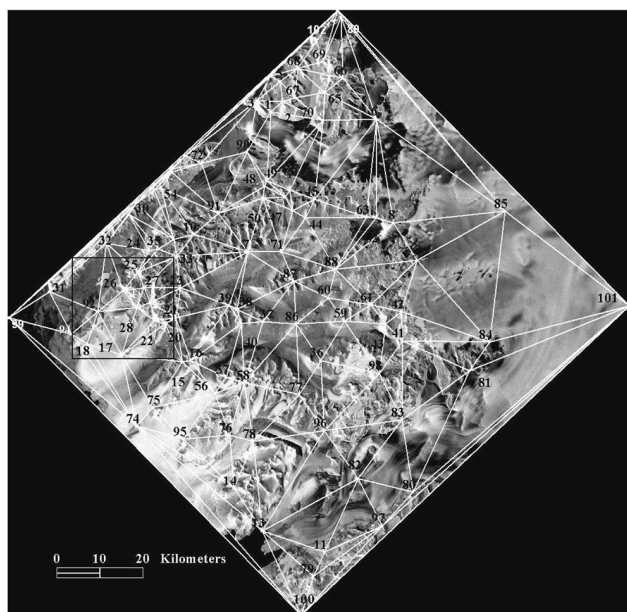
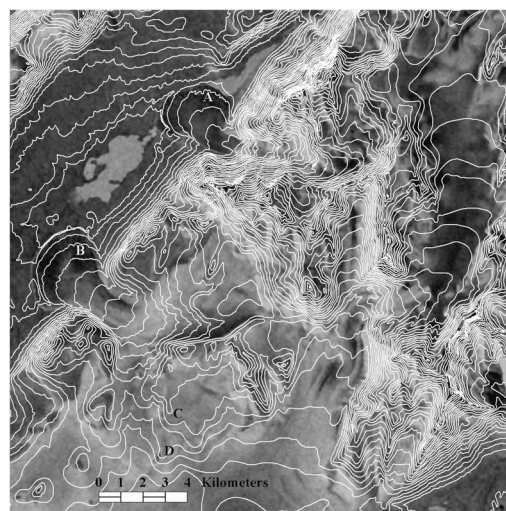


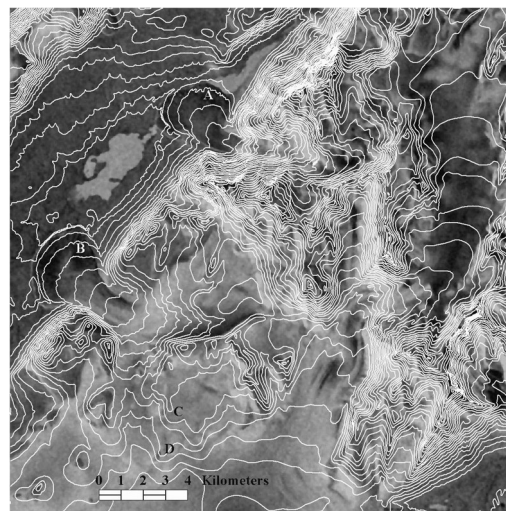
Figure 6. Delaunay triangulation of conjugate points in the Dry Valley region. The background is the orthorectified SAR image.

Among 102 identified conjugate points, the largest positional shift detected is 328 m (Table 2). The average positional shift of conjugate points is 208 m. Although the magnitude of positional shifts varies from 31 m to 328 m, the directions of all shifts are quite consistent (Table 2). In comparison with the Ellsworth Mountains data set described in the following section, the positional shifts in the Dry Valley data set are much smaller and consistent. The reasons are multiple. First, the Dry Valley region has been intensively surveyed over the years, and the topographic data set has a relatively large scale. Second, it is relatively easier to identify horizontal control points in the Dry Valley region because it is close to the McMurdo Scientific Station and rock outcrops exist in the region.

By using Delaunay triangulation based piecewise linear transformation (Figure 6), we geometrically transformed the topographic data set and made it more precisely co-registered with the SAR image data to support the terrain correction operation. As shown in Figure 7, the corrected contour lines closely match the terrain features on the orthorectified SAR image. The improvement on the co-registration is especially evident at



(a)



(b)

Figure 7. Correction of positional errors in topographic data of the Dry Valley region. (a) original contour lines draped on a portion of the orthorectified SAR image indicated by black box in Figure 6; (b) the corrected contour lines draped on a portion of the orthorectified SAR image.

TABLE 2. TEN SELECTED CONJUGATE POINTS WITH THE LARGEST POSITIONAL SHIFTS IN THE DRY VALLEY REGION. COORDINATES OF CONJUGATE POINTS ARE GIVEN IN POLAR STEREOGRAPHIC MAP PROJECTION, AND THEIR LOCATIONS ARE SHOWN IN FIGURE 6

ID	Corrected X-coord	Corrected Y-coord	Original X-coord	Original Y-coord	Shift in X $\Delta X(m)$	Shift in Y $\Delta Y(m)$	Overall shift e(m)
31	378908	-1296267	379139	-1296033	-231	-234	328
47	433564	-1274385	433782	-1274147	-218	-238	323
32	392089	-1285033	392312	-1284809	-223	-224	316
61	453349	-1299256	453596	-1299073	-247	-183	307
36	441805	-1312144	442007	-1311917	-202	-227	304
57	419816	-1316065	420039	-1315859	-223	-206	303
21	408112	-1302240	408282	-1301993	-170	-247	300
8	458604	-1280300	458844	-1280135	-240	-165	291
20	405688	-1303668	405864	-1303437	-176	-231	290
41	460684	-1307600	460882	-1307397	-198	-203	284

locations marked as *A* (Commonwealth Glacier), *B* (Canada Glacier), *C* (nunatak), and *D* (nunatak). Using several reserved conjugate points as checkpoints, it is estimated that the co-registration accuracy is increased to within 50 m after the geometric correction.

Correction of Topographic data in the Ellsworth Mountains, Antarctica

The topographic data source for the Ellsworth Mountains of Antarctica is a contour coverage in the Antarctic Digital Database (ADD) (British Antarctic Survey, 1998). The contour coverage was digitized from a USGS 1:250000 scale Reconnaissance Series map produced using the photogrammetric technique from US Navy tri-camera aerial photographs in 1967. The SAR image used in this example was captured by Radarsat-1 sensor on 29 September, 1997 using the Standard Beam 2 from an ascending orbit (Figure 8a). The terrain in this region is highly variable. The characteristics of the SAR image are shown in Table 1.

As the topographic source data have a relatively coarse resolution (Figure 8b), the identified conjugate points are less dense than the Dry Valley data set. A subset of conjugate points is listed in Table 3. The magnitude of positional errors, indicated by the differences between the original position given in the DEM and the corrected position from the SAR modeling, are as large as 3 to 5 km. Figure 9a shows the displacement vectors of conjugate points identified from four SAR image frames in the Ellsworth Mountains. Clearly, positional shifts are not systematic, and local variation in the magnitude and direction is evident. This implies that the geometric shape of the terrain was distorted in the original topographic data set.

The identified conjugate points are triangulated (Figure 9b), and the positional errors and geometric distortions are successfully corrected using the local piecewise geometric transformation. By using several reserved conjugate points as checkpoints, we estimated that the co-registration accuracy of the corrected DEM with the SAR image is better than 150 m. The corrected DEM was subsequently used for terrain correction and geocoding of the real SAR image to produce the orthorectified SAR image. Figure 10a and 10b compare the original contour map and the corrected contour map with the orthorectified SAR image. The misregistration between the original topographic data and the SAR image is clearly shown in Figure 10a. The corrected topographical data are well co-registered with the SAR image (Figure 10b).

Conclusions and Discussion

In the long history of surveying and mapping, a large volume of topographical maps and digital elevation models has been created at various scales throughout the world. Due to the poor navigation technology and lack of quality geodetic control points in the early years, some historic topographic data

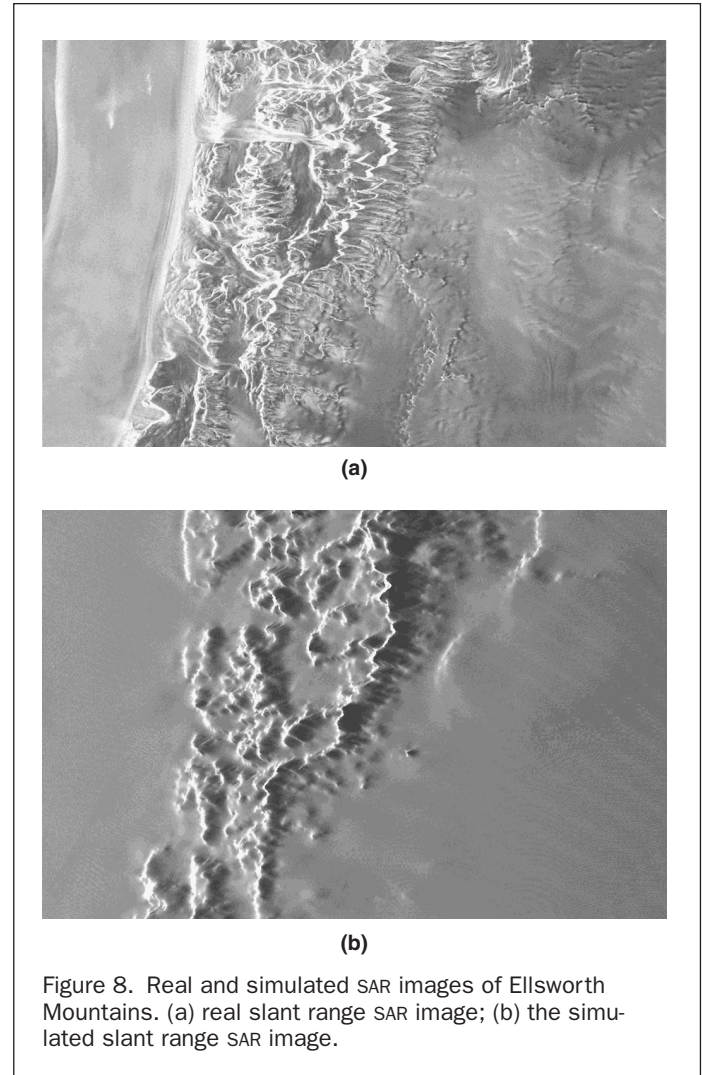


Figure 8. Real and simulated SAR images of Ellsworth Mountains. (a) real slant range SAR image; (b) the simulated slant range SAR image.

sets contain severe positional errors. To make use of the valuable historical topographic data, a technique is required to fix the positional errors. In this paper, we present a new technique for correcting positional errors and geometric distortions in historic topographic maps and their derived digital elevation models. Our technique is based on the rigorous SAR image simulation and mathematical modeling of SAR imaging geometry. Using the Radarsat SAR data, we are able to detect

TABLE 3. TEN SELECTED CONJUGATE POINTS WITH THE LARGEST POSITIONAL SHIFTS IN ELLSWORTH MOUNTAINS. COORDINATES OF CONJUGATE POINTS ARE GIVEN IN POLAR STEREOGRAPHIC MAP PROJECTION, AND THEIR LOCATIONS ARE SHOWN IN FIGURE 9

ID	Corrected X-coord	Corrected Y-coord	Original X-coord	Original Y-coord	Shift in X ΔX (m)	Shift in Y ΔY (m)	Overall shift e (m)
28	-1211411	121399	-1207319	124793	-4092	-3394	5316
8	-1324043	100451	-1328351	99195	4308	1256	4487
13	-1300453	105491	-1304834	104665	4381	826	4459
1	-1359452	96094	-1362957	93480	3505	2614	4373
12	-1304237	111926	-1308448	110766	4211	1160	4368
7	-1341807	99223	-1345893	97835	4086	1388	4314
9	-1308324	92370	-1312498	91617	4174	753	4241
26	-1245942	133241	-1247237	137186	1295	-3945	4153
11	-1288580	90762	-1292408	89368	3828	1394	4074
2	-1373558	88499	-1375519	85213	1961	3286	3827

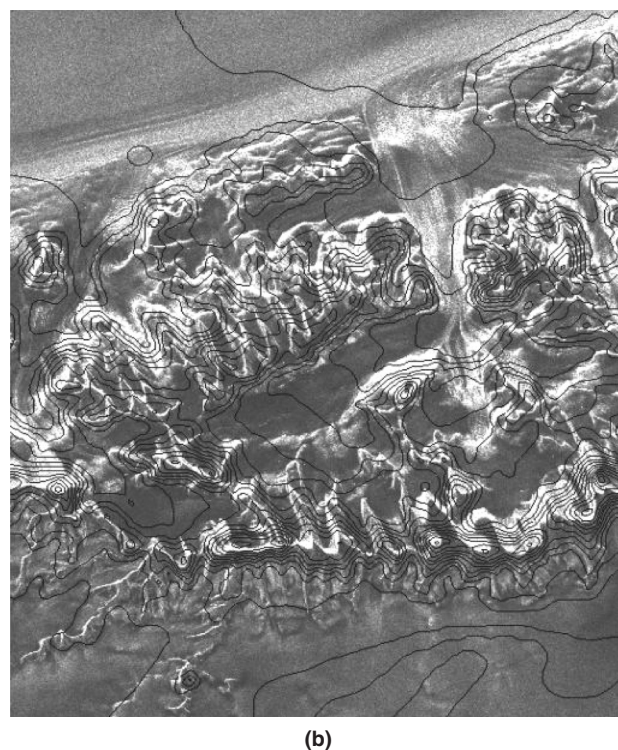
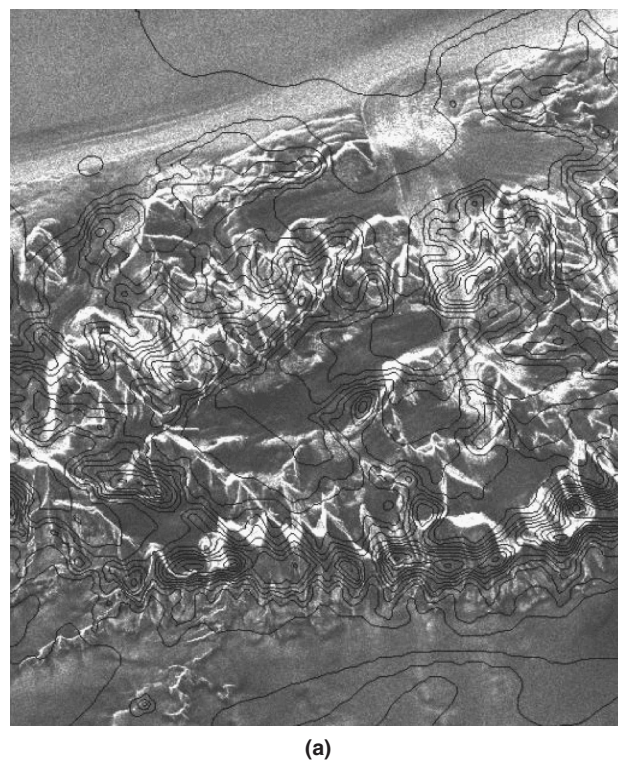
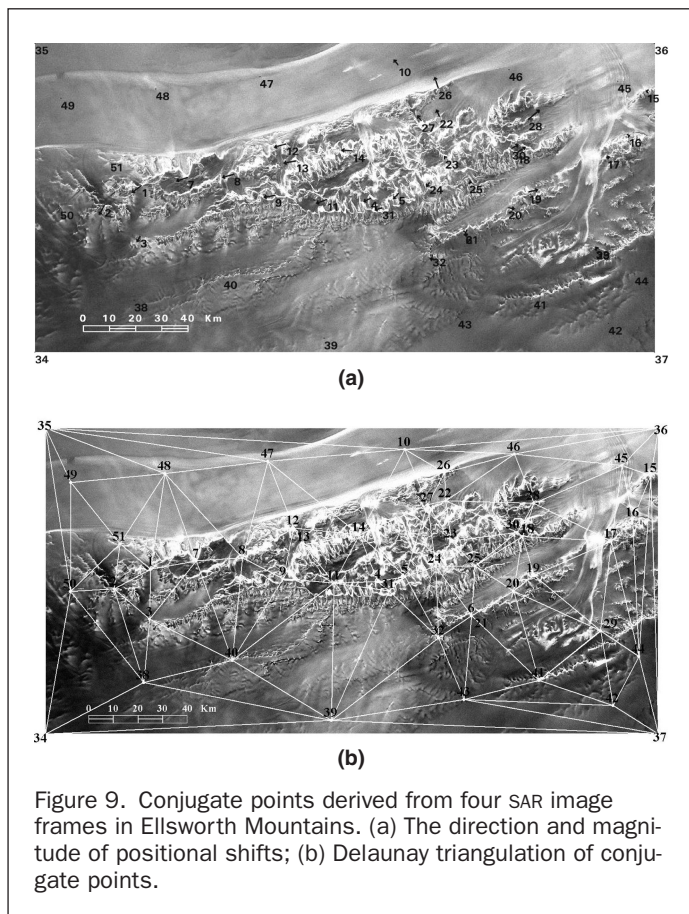


Figure 10. Correction of positional errors and geometric distortions in topographic data of Ellsworth Mountains. (a) Original topographic contour lines draped on the SAR image; and (b) the corrected contour lines draped on the SAR image.

and correct the positional error that is larger than 200 m with the original satellite orbit ephemeris. With the refined satellite orbit ephemeris, the positional error larger than 50 m can be corrected. It should be noted that the achievable positional accuracy with our method also depends on the spatial resolution of the topographical data under correction.

Most previous SAR simulation applications employed available topographic data to refine the satellite ephemeris data for geocoding the real SAR imagery with an assumption that the topographic data are free of positional errors. Our technique is designed to deal with the reverse situation, where the satellite orbit ephemeris information is sufficiently accurate, but serious positional errors exist in the topographical data. Technically, it is more challenging to solve this reverse problem because we need to derive the 3D geographic coordinates for conjugate points. Normally, a stereo pair formed by two real SAR images is required to determine 3D geographic coordinates for the matched conjugate points. With the prior knowledge of the elevation value, we innovatively introduced the earth ellipsoid model equation, which makes it possible to calculate the correct 3D geographic coordinates of conjugate points with a single real SAR image.

The successful application of our technique in the Radarsat Antarctic Mapping Project demonstrates that our technique is effective in correcting the positional errors and geometric distortions in historic topographic data sets. For the Ellsworth Mountains data set, our analysis revealed positional errors of as much as about 5 km. The accuracy assessment shows that our technique has improved the planimetric accuracy of the topographic data to about 150 m. For the Dry Valley data set, the co-registration accuracy of topographic data

with the SAR image data is increased from about 200 m to 50 m after the geometric correction. The enhanced co-registration warrants the correction of terrain distortions inherent in the SAR imagery.

When detected positional shifts of conjugate points are within a small range, it is hard to determine whether the positional error in the topographic data set or the inaccuracy of the satellite orbit ephemeris data is mainly responsible for the shifts. Nevertheless, our technique still provides an alternative to data co-registration in this case. Previous methods commonly co-register the SAR image to the digital elevation model, while our method co-registers the digital elevation model to the SAR image.

Because the acquisition of detailed topographic information is still very costly and time consuming, especially in remote and inaccessible regions and in developing countries, the historical and existing topographic maps still represent important data sources for many applications. With the continuing improvements in satellite orbit ephemeris data, we anticipate an increase in the application of our new technique in the future. It should be noted that our SAR simulation is based on the topography, and the effects of land cover and human structures are not incorporated in the present simulation model. For flat and smooth terrain, it would be difficult to find distinguishable features in the simulated image to be used as conjugate points. Therefore, our technique is more effective for an area with hilly or mountainous terrain.

Acknowledgments

This work was supported by the NASA Grant NAG5-10112 and by the NSF Grant No. 0126149. Radarsat-1 SAR data were provided by the Radarsat: Antarctic Mapping Project of the Byrd Polar Research Center, The Ohio State University. Topographic data for the Dry Valley was provided by C. Hallam of the USGS. The authors want to thank Katy Farness for her assistance in SAR data preparation and Biyan Li for preparing the illustrations.

References

- Arai, K., 1991. GCP acquisition using simulated SAR and evaluation of GCP matching accuracy with texture features, *International Journal of Remote Sensing*, 12:2389–2397.
- British Antarctic Survey, 1998. *Antarctic Digital Database Version 2.0: Manual and Bibliography*, Scientific Committee on Antarctic Research, Cambridge, 74 p.
- Curlander, J.C., and R.N. McDonough, 1991. *Synthetic Aperture Radar Systems and Signal Processing*, John Wiley & Sons, Inc.
- Curlander, J., R. Kwok, and S.S. Pang, 1987. A post-processing system for automated rectification and registration of spaceborne SAR imagery, *International Journal of Remote Sensing*, 8(4):621–638.
- Domik, G., F. Leberl, and J. Cimino, 1986. Multiple incidence angle SIR-B experiment over Argentina: Generation of secondary image products, *IEEE Transaction on Geoscience and Remote Sensing*, 24:492–497.
- Flood, M., 2001. Laser altimetry: From science to commercial LIDAR mapping, *Photogrammetric Engineering & Remote Sensing*, 67(11):1209–1217.
- Fonseca, L., and B.S. Manjunath, 1996. Registration techniques for multisensor remote sensed imagery, *Photogrammetric Engineering & Remote Sensing*, 62(9):1049–1056.
- Goldstein, R.M., H. Engelhardt, B. Kamb, and R. Frolich, 1993. Satellite radar interferometry for monitoring ice sheet motion: Application to an Antarctic ice stream, *Science*, 262:1525–1530.
- Goshtasby, A., 1986. Piecewise linear mapping functions for image registration, *Pattern Recognition*, 19(6):459–466.
- Guidon, B., and H. Maruyama, 1986. Automated matching real and simulated SAR imagery as a tool for GCP acquisition, *Canadian Journal of Remote Sensing*, 12(2):149–158.
- Guidon, B., 1993. Development of a SAR data acquisition planning tool (SARPLAN) based on image simulation, *International Journal of Remote Sensing*, 14:333–344.
- Guidon, B., 1995. Performance evaluation of real-simulated image matching techniques in the acquisition of ground control for ERS-1 image geocoding, *ISPRS Journal of Photogrammetry and Remote Sensing*, 50:2–11.
- Heipke, C., 1992. A global approach for least-squares image matching and surface reconstruction in object space, *Photogrammetric Engineering & Remote Sensing*, 58(3):317–323.
- Hill, J.M., L.A. Graham, and R.J. Henry, 2000. Wide-area topographic mapping and applications using airborne Light Detection and Ranging (LIDAR) technology, *Photogrammetric Engineering & Remote Sensing*, 66(8):908–914.
- Holecz, F., E. Meier, and D. Nüesch, 1993. Postprocessing of relief induced radiometric distorted spaceborne SAR imagery, in G. Schreier (editor), *SAR Geocoding: Data and Systems*, Karlsruhe: Wichmann: 299–352.
- Holtzman, J.C., V.S. Frost, J.L. Abbott, and V.H. Kaupp, 1978. Radar image simulation, *IEEE Transaction on Geoscience Electronics*, GE-16:296–303.
- Jezek, K.C., J. Curlander, R. Barry, F. Carsey, and C. Wales, 1995. *Radarsat: The Antarctic Mapping Project*, Byrd Polar Research Center, Columbus, The Ohio State University.
- Jezek, K.C., and F.D. Carsey, 1993. *Radarsat: The Antarctic Mapping Project*, Byrd Polar Research Center, Report No. 6, ISSN:0896-2472, The Ohio State University.
- Jezek, K.C., 1999. Glaciologic properties of the Antarctic ice sheet from spaceborne synthetic aperture radar observations, *Annals of Glaciology*, 29:286–290.
- Jezek, K.C., 2003. Observing the Antarctic Ice Sheet Using the RADARSAT-1 Synthetic Aperture Radar, *Polar Geography*, 27(3): 197–209.
- Jezek, K., H. Liu, Z. Zhao, and B. Li, 2000. Improving Antarctic Digital Elevation Model by Using Radar Remote Sensing and GIS techniques, *Polar Geography*, 23(3):209–224.
- Kaupp, V., L. Bridges, M. Pizaruck, M. MacDonald, and W. Waite, 1983. Simulation of spaceborne Stereo Radar image experimental Results, *IEEE Transaction on Geoscience and Remote Sensing*, 21: 400–405.
- Kobrick, M., F. Leberl, and J. Raggam, 1986. Radar Stereo Mapping with Crossing Flight Lines, *Canadian Journal of Remote Sensing*, 12(2):132–148.
- Kropatsch, W.G., and D. Strobl, 1990. The generation of SAR layover and shadow maps from digital elevation models, *IEEE Trans. on Geoscience and Remote Sensing*, 28(1):98–107.
- Kwok, R., J.C. Curlander, and S.S. Pang, 1987. Rectification of terrain induced distortion in radar imagery, *Photogrammetric Engineering & Remote Sensing*, 53:507–513.
- Kwok, R., J.C. Curlander, and S.S. Pang, 1990. An automated system for mosaicking spaceborne SAR imagery, *International Journal of Remote Sensing*, 11:209–233.
- Larsgaard, M.L., 1993. *Topographic Mapping of Africa, Antarctica, and Eurasia*, Western Association of Map Libraries, Occasional Paper No. 14.
- Leberl, F., 1990. *Radargrammetric Image Processing*, Artech House, Norwood.
- Leberl, F., 1998. Chapter 4: Radargrammetry, in F.M. Henderson and A.J. Lewis (editors), *Principles & Applications of Imaging Radar*, Manual of Remote Sensing, Third Edition, Volume 2, John Wiley & Sons, Inc., New York.
- Liu, H., K. Jezek, and B. Li, 1999. Development of Antarctic Digital Elevation Model by Integrating Cartographic and Remotely Sensed Data: A GIS-based Approach, *Journal of Geophysical Research*, 104(B10):23,199–23,213.
- Meier, E., U. Frei, and D. Nüesch, 1993. Precise terrain corrected geocoded images, *SAR Geocoding: Data and Systems*, G. Schreier, (editor), Karlsruhe: Wichmann: 173–185.
- Mikhail, E.M., J.S. Bethel, and J.C. McGlone, 2001. *Modern Photogrammetry*, John Wiley & Sons, Inc., 479 p.

- Miller, S.B., and U.V. Helava, 1992. Softcopy photogrammetric workstations, *Photogrammetric Engineering & Remote Sensing*, 58(1): 77–83.
- Naraghi, M., W. Stromberg, and M. Daily, 1983. Geometric rectification of radar imagery using digital elevation models, *Photogrammetric Engineering & Remote Sensing*, 49:195–199.
- Nasr, J., and D. Vidal-Madjar, 1991. Image simulation of geometric targets for spaceborne synthetic aperture radar, *IEEE Transaction on Geoscience and Remote Sensing*, 29(6):986–996.
- Olmsted, C., 1993. *Alaska SAR Facility Scientific SAR User's Guide*, ASF-SD-003, 45 p.
- Polidori, L., and P. Armand, 1995. On the use of SAR image simulation for the validation of relief mapping techniques, *EARSel Advances in Remote Sensing*, 4(2):40–48.
- Polidori, L., 1998. SAR Image Simulation Strategies for Mapping, in T. Schenk and A. Habib (editors), *International Archives of Photogrammetry and Remote Sensing-Object Recognition and Scene Classification from Multispectral and Multisensor Pixels*, 32: 501–507.
- Raggam, J., D. Strobl, and W. Hummelbrunner, 1993. Product quality enhancement and quality evaluation, in G. Schreier (editor), *SAR Geocoding: Data and Systems*, Karlsruhe: Wichmann: 187–205.
- Roth, A., A. Craubner, and T. Hugel, 1993. Standard geocoded ellipsoid corrected images, in G. Schreier (editor), *SAR Geocoding: Data and Systems*, Karlsruhe: Wichmann color, 158–172.
- Saalfeld, A., 1985. A fast Rubber-sheeting transformation using simplicial coordinates, *The American Cartographer*, 12(2):169–173.
- Schenk, T., 1999. *Digital Photogrammetry*, TerraScience. 415 p.
- Schreier, G., 1993. Geometric properties of SAR images, in G. Schreier (editor), *SAR Geocoding: Data and Systems*, Karlsruhe: Wichmann: 103–134.
- Schreier, G., D. Kosmann, and A. Roth, 1990. Design aspects and implementation of a system for geocoding satellite SAR images, *ISPRS Journal of Photogrammetry and Remote Sensing*, 45:1–16.
- Tsai, V.J.D., 1993. Delaunay triangulations in TIN creation: An overview and a linear-time algorithm, *International Journal of Geographic Information Systems*, 7:501–524.
- USGS, 1987. *Digital Elevation Models Data Users Guide*, National Mapping Program, United States Geological Survey, Reston, VA.
- USGS, 1999. *Topographic Mapping*, US Department of the Interior, US Geological Survey, Booklet, 20 p.
- USGS, 2000. *USGS GeoData*, US Department of the Interior, US Geological Survey, 12 p.
- Williams, R.S. Jr., J.G. Ferrigno, C. Swithinbank, B.K. Lucchitta, and B.A. Seekins, 1995. Coastal-change and Glaciological Maps of Antarctica, *Annals of Glaciology*, 21:284–290.
- Wivell, C.E., D.R. Steinwand, G.G. Kelly, and D.J. Meyer, 1992. Evaluation of Terrain Models for the Geocoding and Terrain Correction of Synthetic Aperture Radar (SAR) Images, *IEEE Transaction on Geoscience and Remote Sensing*, 30(6):1137–1144.
- Zebker, H.A., C.L. Werner, P.A. Rosen, and S. Hensley, 1994. Accuracy of topographic maps derived from ERS-1 interferometric radar, *IEEE Transactions on Geoscience and Remote Sensing*, 32:823–836.

(Received 20 September 2002; accepted 22 August 2003; revised 05 September 2003)